

Breaking Spatial Boundaries: Spectral-Domain Registration Guided Hyperspectral and Multispectral Blind Fusion

Kunjing Yang, Libin Zheng, Minru Bai, Ting Lu, *Member, IEEE*, Leyuan Fang, *Senior Member, IEEE*

Abstract—The blind fusion of unregistered hyperspectral images (HSIs) and multispectral images (MSIs) has attracted growing attention recently. To address the registration challenge, most existing methods employ spatial transformations on the HSI to achieve alignment with the MSI. However, due to the substantial differences in spatial resolution of the images, the performance of these methods is often unsatisfactory. Moreover, the registration process tends to be time-consuming when dealing with large-sized images in remote sensing. To address these issues, we propose tackling the registration problem from the spectral domain. Initially, a lightweight Spectral Prior Learning (SPL) network is developed to extract spectral features from the HSI and enhance the spectral resolution of the MSI. Following this, the obtained image undergoes spatial downsampling to produce the registered HSI. In this process, subspace representation and cyclic training strategy are employed to improve spectral accuracy of the registered HSI obtained. Next, we propose a blind sparse fusion (BSF) method, which utilizes group sparsity regularization to equivalently promote the low-rankness of the image. This approach not only circumvents the need for rank estimation, but also reduces computational complexity. Then, we employ the Proximal Alternating Optimization (PAO) algorithm to solve the BSF model, and present its convergence analysis. Finally, extensive numerical experiments on simulated and real datasets are conducted to verify the effectiveness of our method in registration and fusion. We also demonstrate its efficacy in enhancing classification performance.

Index Terms—hyperspectral images, blind fusion, registration, spectral prior learning, group sparse, low-rank.

I. INTRODUCTION

HYPERSPECTRAL images can incorporate tens to hundreds of contiguous spectral bands, granting them the capability to encapsulate a broader swath of the electromagnetic spectrum and providing more nuanced spectral details [1]. Given that different materials exhibit unique reflection signatures, the extensive spectral coverage of HSIs enables precise material identification, which is advantageous in various applications, such as disease monitoring [2], anomaly detection [3], and land cover classification [4].

However, there are fundamental physical limitations that inevitably impose a trade-off between the spatial and spectral

resolution in HSIs [5]. As a result, HSIs typically exhibit low spatial resolution. Moreover, factors such as sensor noise further degrade the quality of the images, limiting their broader applications [6]. In comparison, MSIs exhibit higher spatial resolution but lower spectral resolution. Currently, a mainstream approach to enhancing the spatial resolution of HSIs involves fusing them with high spatial resolution MSIs, which can facilitate the extraction of more intricate and detailed information from the scene [7].

In real-world applications, to achieve high-quality HSI-MSI fusion performance, the HSI and MSI need to be pre-registered. In addition, the spatial and spectral degradation operators, i.e., the point spread function (PSF) and spectral response function (SRF), need to be estimated in advance. To address registration challenges, most existing methods determine geometric spatial transformations by matching spatial feature points between HSIs and MSIs. Then, the transformations are applied to the HSI to achieve alignment with the MSI [8], [9]. However, this procedure, which we refer to as spatial domain registration, has the following limitations: 1) Due to the significant differences in spatial resolution between HSI and MSI, fewer common feature points can be extracted and matched, which often leads to unsatisfactory registration performance in these approaches [10]. 2) The registration process can be generally time-consuming when handling large-sized images in remote sensing [11]. 3) The spatial registration process may potentially introduce distortions to the spectral domain of the HSIs. As a result of these factors, the spatial domain registration methods often fail to efficiently and accurately register the HSIs and MSIs, thereby affecting the subsequent estimation of degradation operators and the fusion process.

To address these issues, we propose solving the HSI-MSI registration problem from the spectral domain. Specifically, a lightweight spectral prior learning (SPL) network is proposed to capture the intrinsic spectral features of the HSIs. Next, we conduct prior-guided spectral super-resolution on the MSI to generate an initial high spatial resolution HSI (HR-HSI). Then, a registered HSI can be obtained after spatially downsampling the HR-HSI, with the option to manually determine the downsampling process, as illustrated in Figure 1. Moreover, we employ subspace representation method [12] to enhance the robustness of the SPL network, and propose a cyclic training strategy (CTS) to alleviate the spectral deviation caused by the misregistration. We refer to this registration approach as spectral domain registration (SDR), which offers the following advantages over spatial domain registration: 1)

Kunjing Yang and Libin Zheng are with the School of Mathematics, Hunan University, Changsha, Hunan 410082, P. R. China (e-mail: kunjing-yang@hnu.edu.cn; fifholz301@hnu.edu.cn).

Minru Bai is the Corresponding author with School of Mathematics, Hunan University, Changsha, Hunan 410082, P. R. China (e-mail: minru-bai@hnu.edu.cn).

Ting Lu and Leyuan Fang are with the College of Electrical and Information Engineering, Hunan University, Changsha 410082, P. R. China (e-mail: tingluhnu@gmail.com; fangleyuan@gmail.com).

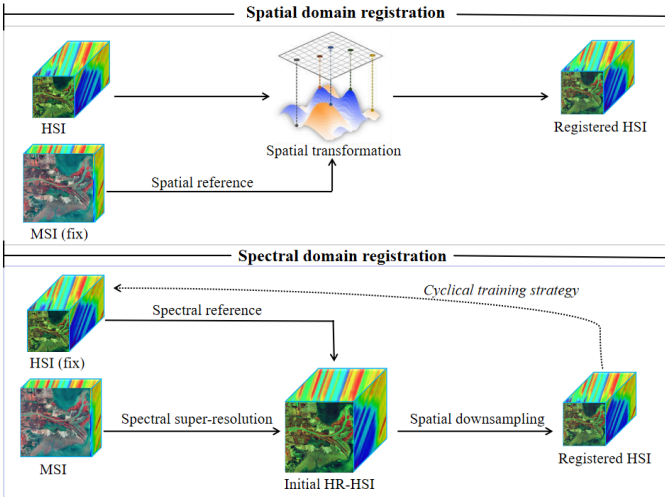


Fig. 1. The comparison of existing spatial domain registration and the proposed spectral domain registration.

Despite the significant difference in spatial resolution between the images, the SDR method can maintain robust and exhibit superior performance compared to spatial domain registration approaches, since the spectral information of the HSI remains well preserved. 2) By tackling registration in spectral domain, the SDR approach enables processing at a substantially reduced scale, thereby significantly decreasing computational time. 3) Through spectral-domain registration, the proposed SDR method can effectively preserve the spectral integrity of HSIs throughout the registration process.

These advantages can be supported by Figure 2, which compares the proposed SDR approach with several well-known registration methods. The results confirm that the SDR method significantly outperforms the other methods in terms of registration performance under a spatial downsampling ratio of 8, where one pixel in the HSI corresponds to 64 pixels in the MSI. In this case, the SDR method achieves an RMSE that is 5.4 units lower than that of X-feat. Moreover, the SDR method requires considerably less computational time.

Subsequently, we propose a subspace representation-based (SR-based) blind sparse fusion (BSF) model to fuse the registered HSI-MSI pairs. *Notably, we only need to estimate the spectral degradation operator since the spatial degradation operator is determined manually.* This reduces the burden of the blind fusion task. To avoid error accumulation, the BSF model performs the fusion and degradation operator estimation tasks simultaneously. The SR-based approaches are generally sensitive to the choice of subspace dimensionality. To address this issue, the proposed BSF model leverages group sparsity to effectively characterize the low-rank structure along the spectral dimension of HSIs. This strategy not only reduces the algorithm's dependence on accurate dimensionality selection, but also avoids the computationally expensive singular value decomposition required by nuclear norm-based regularization methods [13], [14]. Then, we employ the Proximal Alternating Optimization (PAO) algorithm to solve the BSF model and provide its detailed convergence analysis.

The summary of our contributions is outlined as follows:

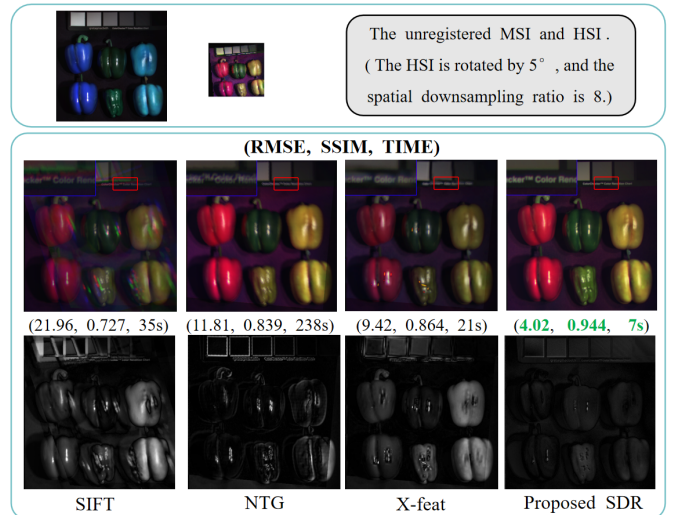


Fig. 2. Image registration results on the 'Peppers' dataset using SIFT [15], NTG [16], X-feat [17] and the proposed SDR. The second row presents the blended images of the registered result and the ground truth, while the third row shows the corresponding difference image.

- We propose a novel spectral domain registration (SDR) method. Specifically, a lightweight SPL network is developed, which generates a registered HSI by performing spectral super-resolution on the MSI. In this process, we employ the subspace representation (SR) approach to enhance the robustness of the SDR method. Moreover, a cyclic training strategy (CTS) is proposed to further alleviate spectral distortion in the registered HSI.
- We propose the BSF model for the blind fusion task, which only requires estimating the spectral degradation operator. Furthermore, the BSF model utilize group sparsity to equivalently characterize the low-rankness, which not only reduces the algorithm's sensitivity to rank selection but also decreases the computational complexity.
- We solve the BSF model using PAO algorithm and provide its detailed convergence analysis. Extensive numerical experiments are conducted on simulated and real-world HSI datasets to verify the efficacy of our proposed method in registration, fusion, and enhancing classification accuracy. Moreover, our approach requires considerably less time than competing methods.

The remaining sections of this paper are organized as follows. Related work is introduced in section II. In section III, we propose the SDR-BSF method. Then in section IV, numerical experiments on HSI-MSI registration and fusion are presented. Finally, we make a conclusion in section V.

II. RELATED WORK

A. HSI-MSI fusion

Existing HSI-MSI fusion approaches can primarily be categorized into three types: matrix factorization (MF)-based, tensor factorization (TF)-based and deep learning-based methods [18]. MF-based methods explore the internal correlations within images to reduce problem dimensions or perform component separation. Yokoya *et al.* [19] proposed a coupled non-negative matrix factorization fusion method based on a linear

spectral mixture model. The work in [12] proposed a subspace representation method that exploits the strong correlations within the spectral dimensions of HSI to achieve significant dimensionality reduction of the fusion model. Dong *et al.* [20] developed a Nonnegative Structured Sparse Representation (NSSR) method which jointly estimates the dictionary and the sparse coefficients.

Recently, TF-based methods have shown superior fusion performance by leveraging the multilinear features of the data [21]. The target HSI was restructured as a CP approximation in work [22], and an alternating least squares algorithm called Super-resolution Tensor REconstruction (STEREO) was developed. Zeng *et al.* [23] utilized CP factorization to characterize the low-rank structure of HSIs with a sparse Bayesian framework for adaptive rank determination. Li *et al.* [24] proposed a methodology employing coupled sparse Tucker factorization (CSTF) for HSI-MSI fusion. The work in [25] integrated linear unmixing with low Tensor-Train decomposition into the fusion model, incorporating a sparse prior to enhance the fusion process. Xu *et al.* [26] employed a tensor-product (t-product) to decompose the target HSI and utilized non-local clustering sparse representation method.

Deep learning-based methods employ neural networks to extract intrinsic features from HSI and MSI data, then synthesizing a fused image that effectively integrates the spatial details and spectral characteristics from both datasets [27] [28]. Palsson *et al.* [29] used a 3D convolutional neural network to fuse the HSI and MSI, while reduced the dimension of HSI by using principal component analysis. Dian *et al.* [30] incorporated a subspace representation method into a plug-and-play framework, in which a CNN-based denoiser is integrated into the ADMM algorithm as the proximity operator. Xie *et al.* [31] proposed an interpretable fusion network by unfolding the proximal gradient algorithm to solve the model, which facilitates an easy intuitive observation and analysis on what happens inside the network. Wang *et al.* [32] developed a spatial-spectral implicit neural representation fusion network to adequately restore the continuous spatial and spectral information of the images. Liu *et al.* [33] proposed a low-rank Transformer network (LRTN) for HSI-MSI fusion, exploiting both the intrinsic correlations and the global spatial correlations within images.

The aforementioned fusion methods generally assume that the spatial and spectral degradation operators are known. In practice, however, these operators may be unknown, which is referred to as blind fusion [22]. Several alternating optimization algorithms have been proposed to specifically estimate the degradation operators under accurate registration conditions [12], [34]. To prevent error accumulation, Yang *et al.* [13] incorporated triple decomposition and the estimation of the degradation operators simultaneously with the fusion task. Moreover, some approaches leverage the powerful nonlinear fitting capabilities of neural networks to design modules that approximate the spatial and spectral degradation processes [35], [36]. Wang *et al.* [37] developed an unsupervised blind fusion method based on Tucker decomposition and spatial-spectral manifold learning.

B. Registration-fusion method

Due to the fact that HSIs and MSIs are typically captured by different sensors, the image pairs obtained in practice are often unregistered, which severely affects the subsequent fusion process. This has prompted researchers to jointly address the challenges of registration and fusion. In the case where the degradation operators are known, Fu *et al.* [38] presented an effective approach for simultaneous HSI super-resolution and geometric alignment of the image pair, which incorporates spectral dictionary learning and sparse coding methods. Ying *et al.* [39] introduced a new registration method named NED for clear-blur image similarity measurement and incorporated interpolation into the fusion process. For cases where the degradation operators are unknown, the task of registration and fusion becomes even more challenging. Recently, some deep learning-based methods have been proposed. Qu *et al.* [10] developed an unregistered and unsupervised mutual Dirichlet-Net (u2-MDN), which employed a collaborative $l_{2,1}$ norm as the reconstruction error. Zheng *et al.* [9] embed the linear spectral unmixing method into the fusion network and introduced the STN [40] as the registration module within the network. Guo *et al.* [41] developed a stereo cross-attention network based on a Transformer to extract the abstract features of the unregistered images, then reconstruct to obtain the fused image. In [42], a multi-scale registration-fusion consistency physical perception model (RFCM) is developed, which leverages optimization algorithms to guide the fusion process.

III. THE PROPOSED SDR-BSF METHOD

The HSIs and MSIs can be considered as 3-D tensors. We represent the target HR-HSI as $\mathcal{X} \in \mathbb{R}^{M \times N \times H}$, where M and N denote the two spatial dimensions, and H represents the number of spectral bands. Similarly, the obtained HSIs and MSIs are denoted as $\mathcal{Y} \in \mathbb{R}^{m \times n \times h}$ and $\mathcal{Z} \in \mathbb{R}^{M \times N \times h}$, respectively, where $m < M$, $n < N$, and $h < H$. We denote $\mathbf{X} \in \mathbb{R}^{H \times MN}$, $\mathbf{Y} \in \mathbb{R}^{H \times mn}$, and $\mathbf{Z} \in \mathbb{R}^{h \times MN}$ as the mode-3 unfolding matrices [43] of \mathcal{X} , \mathcal{Y} and \mathcal{Z} , respectively.

The derived HSI \mathbf{Y} can be perceived as a spatially degraded variant of the target HR-HSI \mathbf{X} . Therefore, the relationship between \mathbf{Y} and \mathbf{X} can be expressed as:

$$\mathbf{Y} = \mathbf{XBS} + \mathbf{N}_1, \quad (1)$$

where $\mathbf{B} \in \mathbb{R}^{MN \times MN}$ is a spatial blurring matrix representing the hyperspectral sensor's point spread function (PSF), which is assumed band-independent and operates under circular boundary conditions [12], $\mathbf{S} \in \mathbb{R}^{MN \times mn}$ is a downsampling matrix. Matrix \mathbf{N}_1 represents the noise, with the assumption that it follows the Gaussian distribution. Similarly, the MSI \mathbf{Z} can be considered as the degraded version of \mathbf{X} along the spectral mode. The relationship can be expressed as:

$$\mathbf{Z} = \mathbf{RX} + \mathbf{N}_2, \quad (2)$$

where $\mathbf{R} \in \mathbb{R}^{h \times H}$ is the spectral response matrix and depends on the spectral response function (SRF) of sensor, \mathbf{N}_2 denotes the Gaussian noise contained in the observed MSI.

Equations (1) and (2) may not hold true simultaneously since \mathbf{Y} and \mathbf{Z} might not be properly registered. The existing

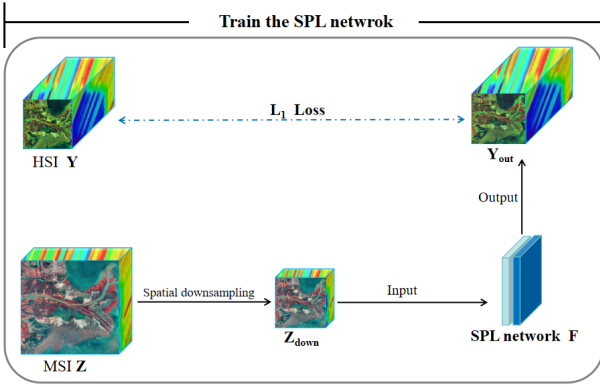


Fig. 3. The procedure of training the SPL network.

registration process typically treats the MSI \mathcal{Z} as the reference and applies a spatial transformation τ to the HSI \mathcal{Y} . The registered HSI, denoted as \mathcal{Y}_R , is then defined as:

$$\mathcal{Y}_{R(i)} := \mathcal{Y}_{(i)}(\tau[x, y]), \quad i = 1, 2, \dots, H, \quad (3)$$

where $\mathcal{Y}_{(i)}$ denotes the i -th spectral band. However, due to factors such as significant differences in image spatial resolution, most image registration methods generally cannot achieve satisfactory accuracy [8]. Moreover, the process of spatial registration is frequently time-consuming and may potentially introduce deviations in the spectral dimension of the HSIs. Therefore, we consider whether the registration problem can be addressed from the spectral domain. From this point, we propose to fix the HSI and transform the MSI, allowing the HSI to provide spectral prior information for MSI spectral super-resolution. In this way, we can obtain a preliminary HR-HSI. After spatial downsampling, we obtain a new HSI that, theoretically, is precisely registered with the MSI.

The first challenge is: how to leverage the spectral information from the HSI to guide spectral super-resolution on the MSI. Our approach is to learn a mapping that transforms the MSI into HSI. This mapping, denoted as $\mathcal{F} : \mathbb{R}^{n_1 \times n_2 \times h} \rightarrow \mathbb{R}^{n_1 \times n_2 \times H}$, functionally serves as the inverse of the spectral response operator \mathbf{R} in equation (2). However, \mathbf{R} is a matrix with far more columns than rows, rendering it devoid of a true inverse matrix. Therefore, we use a neural network to approximate the mapping \mathcal{F} , which is referred to as the spectral prior learning (SPL) network. Once trained, the SPL network will be employed to perform spectral super-resolution on the MSI \mathcal{Z} , yielding an initial HR-HSI. By spatially downsampling the HR-HSI, we can obtain a registered HSI \mathcal{Y}_R . Finally, we fuse \mathcal{Y}_R and \mathcal{Z} using the BSF model. The specific workflow is as follows:

Step 1: Train the SPL network. Firstly, we spatially downsample the MSI to align its spatial dimensions with those of the HSI. Using a Python command, we denote:

$$\mathcal{Z}_{down} := \mathcal{Z}[1 : M : d, 1 : N : d, :], \quad (4)$$

where d represents the downsampling ratio. Then, we input \mathcal{Z}_{down} into the network \mathcal{F} for spectral super-resolution, yielding another HSI, denoted as \mathcal{Y}_{out} , i.e., $\mathcal{Y}_{out} = \mathcal{F}(\mathcal{Z}_{down})$. The loss function is defined as:

$$Loss := \|\mathcal{Y}_{out} - \mathcal{Y}\|_{l_1}. \quad (5)$$

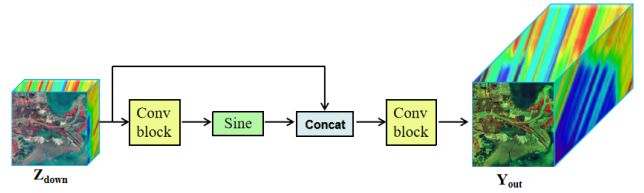


Fig. 4. The architecture of the SPL Network.

where $\|\cdot\|_{l_1}$ is the l_1 norm. The procedure of training the SPL network is illustrated in Figure 3. Our objective is to ensure that \mathcal{Y}_{out} is as spectrally similar to \mathcal{Y} as possible. Therefore, we employ spatial cropping technique to highlight the spectral dimension information while increasing the amount of training data. Finally, we optimize the network parameters using adaptive moment estimation (Adam) [44] algorithm.

Step2: Obtain registered HSIs. By inputting the original MSI \mathcal{Z} into the trained network \mathcal{F} , we can obtain an initial HR-HSI $\mathcal{F}(\mathcal{Z})$. Subsequently, we spatially downsample $\mathcal{F}(\mathcal{Z})$ to obtain a registered HSI, which is denoted as:

$$\mathcal{Y}_R := \mathbf{Fold}_3((\mathcal{F}(\mathcal{Z})_{(3)})\widehat{\mathbf{B}}\mathbf{S}), \quad (6)$$

where $(\cdot)_{(3)}$ represents the mode-3 unfolding matrix of a tensor and $\mathbf{Fold}_3(\cdot)$ denotes its inverse operator. Here, we can choose the blur kernel $\widehat{\mathbf{B}}$ manually. Typically, we choose the kernel $\widehat{\mathbf{B}}$ that is much stronger than the original \mathbf{B} , so that the effect of \mathbf{B} becomes negligible. Then, the obtained \mathcal{Y}_R is spatially registered with the MSI \mathcal{Z} since it comes from $\mathcal{F}(\mathcal{Z})$.

Step3: Blind fusion. We utilize the BSF model to perform blind fusion on \mathcal{Y}_R and \mathcal{Z} , which do not need to estimate the blur kernel since we have pre-set $\widehat{\mathbf{B}}$ in (6). \square

The SPL network \mathcal{F} comprises a residual network constructed with two layers of convolutions, as shown in Figure 4. The activation function Sine [45] is applied in our network to enhance its nonlinear fitting capability.

A. Improving the spectral domain registration (SDR) process

Since the initial HSI \mathcal{Y} and MSI \mathcal{Z} are not registered, the above SDR process may introduce spectral deviations, resulting in inaccuracies in the spectral information of the obtained \mathcal{Y}_R . Moreover, the spectral super-resolution process lacks sufficient robustness to noise. Therefore, **the second challenge is: how to improve the accuracy and robustness of spectral domain registration process.**

1) *Enhance the robustness of SDR:* HSIs typically exhibit strong spectral correlations. *Considering that \mathcal{Y}_R primarily inherits the spectral information from \mathcal{Y} , they should approximately lie in the same spectral subspace.* Therefore, we leverage subspace representation (SR) method [12], which projects the HSI \mathcal{Y} into a lower-dimensional subspace:

$$\mathcal{Y} = \mathcal{A} \times_3 \mathbf{D}, \quad (7)$$

where $\mathcal{A} \in \mathbb{R}^{M \times N \times L}$ is the coefficient tensor, $\mathbf{D} \in \mathbb{R}^{H \times L}$ denotes the dictionary and L represents the dimension of the subspace spanned by the columns of \mathbf{D} . The ‘ \times_3 ’ represents the mode-3 tensor-matrix product [43]. Regarding the selection of the dictionary \mathbf{D} , we employ the classical Truncated-SVD method, which is outlined as follows:

$$[\mathbf{U}, \Sigma, \mathbf{V}] = \text{svd}(\mathbf{Y}) \quad \text{and} \quad \mathbf{D} = \mathbf{U}(:, 1 : L), \quad (8)$$

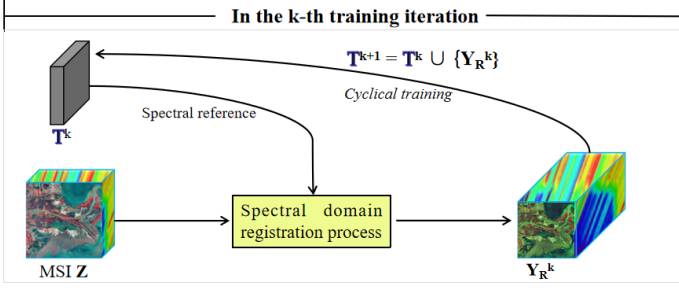


Fig. 5. The flowchart of the cyclic training strategy (CTS).

where Σ denotes the matrix whose diagonal elements are the singular values of \mathbf{Y} , \mathbf{U} and \mathbf{V} are the left and right singular matrices, respectively. Then, we project \mathcal{Y}_{out} into the subspace, which can be expressed as:

$$\mathcal{Y}_{out} = \mathcal{A}_{out} \times_3 \mathbf{D}, \quad (9)$$

where $\mathcal{A}_{out} \in \mathbb{R}^{M \times N \times L}$ is the coefficient tensor. In this way, we only need to learn the mapping from MSI to the coefficient tensor, denoted as $\mathcal{G} : \mathbb{R}^{n_1 \times n_2 \times h} \rightarrow \mathbb{R}^{n_1 \times n_2 \times L}$. The relationship can be expressed as

$$\mathcal{A}_{out} = \mathcal{G}(\mathcal{Z}_{down}), \quad \mathcal{F}(\cdot) = \mathcal{G}(\cdot) \times_3 \mathbf{D}. \quad (10)$$

The loss function is defined as $\|\mathcal{A} - \mathcal{A}_{out}\|_{l_1}$. Since L is typically much smaller than H , training the network $\mathcal{G}(\cdot)$ is more efficient than directly training $\mathcal{F}(\cdot)$. Therefore, the SR method can not only enhance the robustness of the model, but also improve the efficiency of spectral super-resolution.

2) *Mitigating \mathcal{Y}_R 's spectral deviation*: In fact, the original HSI \mathcal{Y} possesses accurate spectral information but is spatially misregistered with respect to the MSI \mathcal{Z} . Conversely, the \mathcal{Y}_R we obtain is spatially registered with the MSI \mathcal{Z} , but its spectral information is potentially biased. *Both possess part of the desired properties*. Therefore, we propose a cyclic training strategy (CTS), which involves incorporating the generated \mathcal{Y}_R from each iteration into the training set, allowing the network to undergo repeated training. Specifically, we denote the training set as \mathbb{T} . Initially, we define $\mathbb{T}^0 = \{\mathcal{Y}\}$. At the end of each training iteration, we incorporate the obtained \mathcal{Y}_R into the training set \mathbb{T} , i.e.,

$$\mathbb{T}^{k+1} = \mathbb{T}^k \cup \{\mathcal{Y}_R^{(k)}\}, \quad k = 0, 1, 2, \dots, \quad (11)$$

where $\mathcal{Y}_R^{(k)}$ represents the output of the k -th training iteration, as shown in Figure 5. Through this iterative training strategy, we can obtain a sufficient amount of training data to train a more stable and higher-quality network. As a result, the final obtained \mathcal{Y}_R not only maintains spatial registration but also exhibits significantly enhanced spectral accuracy.

Finally, by integrating 1) and 2), we project each element in \mathbb{T} into the subspace spanned by \mathbf{D} in each training iteration. Therefore, the actual training set in the k -th training iteration is:

$$\mathbb{T}_{\mathbf{D}}^k := \{\mathcal{Y} \times_3 \mathbf{D}^T \mid \mathcal{Y} \in \mathbb{T}^k\}, \quad (12)$$

and we minimize the l_1 loss between \mathcal{A}_{out} and $\mathbb{T}_{\mathbf{D}}^k$. The entire training process is summarized in Algorithm 1.

Algorithm 1 The procedure of the SDR method.

Input: \mathcal{Y} , \mathcal{Z} , \mathbf{D} .

Initialize: $\mathbb{T}^0 = \{\mathcal{Y}\}$, \mathcal{Z}_{down} . Set $k = 0$.

1: Obtain \mathcal{A}_{out} : $\mathcal{A}_{out} = \mathcal{G}(\mathcal{Z}_{down})$;

2: Update the set $\mathbb{T}_{\mathbf{D}}^k$ by (12);

3: Train the SPL network \mathcal{G} to minimize the l_1 loss between \mathcal{A}_{out} and the set $\mathbb{T}_{\mathbf{D}}^k$;

4: Obtain the HR-HSI, i.e., $\mathcal{F}(\mathcal{Z}) = \mathcal{G}(\mathcal{Z}) \times_3 \mathbf{D}$;

5: Obtain $\mathcal{Y}_R^{(k)}$ by downsampling $\mathcal{F}(\mathcal{Z})$ as described in (6);

6: Update set \mathbb{T}^{k+1} as (11);

7: If the maximum iteration count has not been reached, set $k = k + 1$ and return to step 1;

Output: \mathcal{Y}_R^k .

Remark 3.1: When dealing with significant unregistered scale discrepancies, performing a coarse pre-registration of the images prior to applying the SDR method can generally enhance its registration performance. This approach is particularly applicable to remote sensing geo-images that allow pre-registration based on geographic coordinates.

B. The blind sparse fusion (BSF) method

Next, we propose the BSF model to obtain the final fused image. Unless otherwise specified, \mathbf{Y} , \mathcal{Z} and \mathbf{X} will represent the mode-3 unfolding matrices of \mathcal{Y}_R , \mathcal{Z} and \mathcal{X} , respectively.

Considering the strong correlation between different spectral bands of HSI, we leverage subspace representation method for \mathbf{X} , i.e.,

$$\mathbf{X} = \mathbf{D}\mathbf{A}, \quad (13)$$

where $\mathbf{D} \in \mathbb{R}^{H \times r}$ and $\mathbf{A} \in \mathbb{R}^{r \times MN}$. The matrix \mathbf{D} is directly defined as equation (8). However, the fusion methods based on (13) are typically sensitive to the choice of r . Some approach involves utilizing the nuclear norm-based regularizer to promote low-rank properties [13], [14], which leads to high-quality reconstructions without the need to estimate r . Nevertheless, solving the subproblem requires performing SVD repeatedly, which is computationally expensive. To address these issues, we utilize the following theorem.

Theorem 3.1: [46] For any matrix $\mathbf{X} \in \mathbb{R}^{m \times n}$ with $\text{rank}(\mathbf{X}) \leq r$, we have

$$\text{rank}(\mathbf{X}) = \min_{\mathbf{X}=\mathbf{D}\mathbf{A}} \|\mathbf{D}^T\|_{2,0} = \min_{\mathbf{X}=\mathbf{D}\mathbf{A}} \|\mathbf{A}\|_{2,0}, \quad (14)$$

with $\mathbf{D} \in \mathbb{R}^{m \times r}$ and $\mathbf{A} \in \mathbb{R}^{r \times n}$. Here $\|\mathbf{A}\|_{2,0} := \sum_i \|\mathbf{a}_i\|_F^0$ (adopting the convenience that $0^0 = 0$) denotes the number of non-zero rows of \mathbf{A} (\mathbf{a}_i represents the i th row of \mathbf{A} and $\|\cdot\|_F$ represents the Frobenius norm).

Theorem 3.1 implies that *even if the chosen r is relatively large, we can leverage group sparsity regularization to promote the low-rank property of the target \mathbf{X} , thereby reducing the dependence on the selection of parameter r* . Therefore, we propose the blind sparse fusion (BSF) model as follows:

$$\begin{aligned} \min_{\mathbf{A}, \mathbf{R}} & \|\mathbf{D}\mathbf{A}\mathbf{B} - \mathbf{Y}\|_F^2 + \|\mathbf{R}\mathbf{D}\mathbf{A} - \mathbf{Z}\|_F^2 + \alpha \|\mathbf{A}\|_{2,\psi}, \\ \text{s.t.} & \quad \mathbf{R} \geq 0, \end{aligned} \quad (15)$$

where α is the weight parameter, and $\|\mathbf{A}\|_{2,\psi} := \sum_i \psi(\|\mathbf{a}_i\|)$ is the non-convex relaxation of $\|\mathbf{A}\|_{2,0}$. The function ψ can be chosen as the CapL1 function, which is defined as $\psi_\rho(x) = \min\{1, \frac{x}{\rho}\}$ for a fixed parameter $\rho > 0$. According to [47], the proximal mapping of $\|\cdot\|_{2,\psi}$ is

$$\text{prox}_{\lambda\psi}(x) = \begin{cases} (\|x\| - \frac{\lambda}{\rho})_+ \frac{x}{\|x\|}, & \text{if } \|x\| \leq \rho + \frac{\lambda}{2\rho}, \\ x, & \text{otherwise,} \end{cases} \quad (16)$$

where $(\cdot)_+ := \max\{\cdot, 0\}$. The complexity of computing (16) is much lower than that of computing the proximal operator of the nuclear norm [48]. Note that we only need to estimate the spectral degradation operator \mathbf{R} , which avoids the BSF model becoming more ill-posed.

To solve the BSF model, we employ the Proximal Alternating Optimization (PAO) algorithm. For convenience, we denote the objective function of the BSF model as $g(\mathbf{A}, \mathbf{R})$. In the k -th iteration, we add proximal terms to the objective function for each variable. The iterative scheme of PAO is

$$\mathbf{A}^{k+1} = \arg \min_{\mathbf{A}} g(\mathbf{A}, \mathbf{R}^k) + \frac{\lambda}{2} \|\mathbf{A} - \mathbf{A}^k\|_F^2, \quad (17)$$

$$\mathbf{R}^{k+1} = \arg \min_{\mathbf{R}} g(\mathbf{A}^{k+1}, \mathbf{R}) + \frac{\lambda}{2} \|\mathbf{R} - \mathbf{R}^k\|_F^2, \quad (18)$$

where $\lambda > 0$ denotes the proximal parameter. We update variables \mathbf{A}^{k+1} and \mathbf{R}^{k+1} alternatively. The PAO algorithm for solving the BSF model is summarized in Algorithm 2.

Algorithm 2 PAO algorithm for solving the BSF model

Input: \mathbf{Y} , \mathbf{Z} , α , ρ and λ .

Initialize: \mathbf{A}^k and \mathbf{R}^k . Set $k = 0$.

1: Update \mathbf{A}^{k+1} by solving the subproblem (17);

2: Update \mathbf{R}^{k+1} by solving the subproblem (18);

3: If the termination criterion is not met,

set $k = k + 1$ and return to step1;

Output: $\mathbf{X} = \mathbf{D}\mathbf{A}^{k+1}$.

Next, we present the convergence analysis of the algorithm.

Theorem 3.2: Let $\{\mathcal{P}^k = (\mathbf{A}^k, \mathbf{R}^k)\}_{k \in \mathbb{N}}$ be the sequence generated by Algorithm 2. If $\{\mathcal{P}^k\}_{k \in \mathbb{N}}$ is bounded, then $\{\mathcal{P}^k\}_{k \in \mathbb{N}}$ converges to a critical point of the objective function of model (15) and

$$\sum_{k=0}^{+\infty} \|\mathcal{P}^{k+1} - \mathcal{P}^k\| < +\infty.$$

The detailed process of the algorithm and the convergence analysis are included in the supplementary materials.

From the conclusion of the Theorem 3.2, we can deduce that $\lim_{k \rightarrow +\infty} \|\mathcal{P}^{k+1} - \mathcal{P}^k\| = 0$. Therefore, the relative change between two consecutive steps can be directly employed as the termination criterion for the PAO algorithm.

IV. NUMERICAL EXPERIMENTS

In this section, we evaluate the proposed SDR-BSF method through a series of experiments conducted on publicly available HSI datasets. Initially, to assess the registration perfor-

mance of the SDR method, we compare it with: the feature-based SIFT [15], intensity-based NTG [16], and deep learning-based X-feat [17] approaches. Meanwhile, two blind fusion algorithms, TriD [13] and ZSL [34], are selected to fuse aligned image pairs to validate the overall effectiveness of the proposed SDR-BSF method. Next, we compare the SDR-BSF method with several well-known fusion methods on both simulated and real datasets. These methods include model-driven approaches: Hysure [12], Integrated [11], and NED [39], as well as deep learning-based methods: NonregSR [9], PMIRFCo [49], DFMF [50], HPWRL [51] and IR-ArF [52]. Finally, ablation studies are conducted to validate the effectiveness of each novel component in our approach.

A. Datasets

1). Simulated datasets.

(a). Pavia University and Pavia Center [53]: The Pavia University and Pavia Center datasets, following processing, respectively encompass 103 and 102 spectral bands, each spanning a wavelength spectrum from 0.43 μm to 0.86 μm . We select 93 bands from both scenes and crop a region of interest from the up-left corner, resulting in the image size of 256 \times 256 \times 93. To generate the HSIs, we apply the spatial downsampling with scale factor (**sf**) of 4 and 8 to the Pavia Center and Pavia University, respectively. Additionally, the HR-MSI is generated using a four-band IKONOS-like reflectance spectral response filter [54].

(b). CAVE¹: The CAVE dataset comprises images with 31 bands, spanning the spectral range from 400 nm to 700 nm at 10 nm intervals. All images within the dataset were uniform in dimensions, measuring 512 \times 512 \times 31. We selected the ‘Face’, ‘Superballs’ and ‘Toys’ images for our experiments. Specifically, the spatial dimensions of the ‘Face’ were downsampled by a scale factor (**sf**) of 8, whereas those of the ‘Superballs’ image were downsampled by **sf** = 16. The ‘Toys’ was downsampled by **sf** = 32. We obtained the MSIs with three bands by the Nikon D700 camera², i.e., $h = 3$.

2). Real-world Dataset.

(c). GF1-GF5 [41]: In the GF1-GF5 dataset, the size of HSI is 1161 \times 1129 \times 150, and the size of MSI is 2322 \times 2258 \times 4. For the HSI, we select bands 11 to 100 and extract a 1024 \times 1024 pixel area from the top-left quadrant, using a sampling ratio of 8, resulting in a HSI with dimensions of 128 \times 128 pixels across 90 bands. Concurrently, a 2048 \times 2048 pixel segment was taken from the same top-left corner of the MSI, employing a sampling interval of 4, which produced a MSI with dimensions of 512 \times 512 pixels and 4 bands.

(d). FR2 [55]: The Panchromatic (Pan) image and HSI of the full resolution dataset FR2 have been obtained by extracting a 12km \times 12km portion (2400 \times 2400 pixels for Pan image and 400 \times 400 \times 63 pixels for HSI) from the original 30km \times 30km PRISMA acquisition. In our experiments, we spatially downsampled the Pan image and HSI by a factor of 4. This resulted in an HSI with dimensions of 100 \times 100 pixels and 63 bands, and a Pan image with a size of 600 \times 600 pixels.

¹<https://www.cs.columbia.edu/CAVE/databases/multispectral/>

²https://maxmax.com/spectral_response.htm

B. Implementation Details

Subsequently, we provide a description of our experimental details and the associated settings.

Unregistered settings. For the unregistered case, to quantitatively compare evaluation metrics, we manually introduce deformations to generate unaligned images for comparison. Specifically, we apply three types of transformations to each band of the HSI, including:

- Scaling: we enlarge each band of the HSI by 1.1 times.
- Rotation: we rotate each band of the HSI by 2 degrees.
- Pincushion Distortion: we apply pincushion distortion to each band of the HSI to simulate common distortions at the edges of the camera’s field of view (nonlinear). The scale of the distortion is quantified by a distortion coefficient, which we set to 1×10^{-2} .

The spatial dimensions of the HSI typically change after undergoing various transformations, and we crop the images back to their original size.

In addition to simulation experiments, we also conducted tests on real-world datasets: GF1-GF5 and FR2. The images in the GF1-GF5 dataset are unregistered, while the images from the FR2 dataset have undergone pre-registration. To increase the degree of misregistration, we artificially introduced local pincushion distortions to the HSI in FR2 dataset. Furthermore, both the spatial and spectral degradation operators are unknown for the two datasets.

Parameter settings. For the SPL network, the convolution kernel size is typically set within the range of 3 to 9, with zero-padding applied. Generally, the greater the degree of misregistration, the larger the convolution kernel size should be, as this allows the network to capture feature correlation over a wider range. The subspace dimension L is set to 10. For the BSF model, we set $\alpha = 2 \times 10^{-1}$, $\nu = 2$ and $\lambda = 1 \times 10^{-3}$. The parameter r is set within [2, 6].

Evaluation metrics. To assess the quality of the reconstructed HSI, we choose the following evaluation metrics: peak signal-to-noise ratio (PSNR) [56], structural similarity (SSIM) [56], relative dimensionless global error in synthesis (ERGAS) [57], spectral angle mapper (SAM) [57] and root mean square error (RMSE) [57]. We also compared the time consumption of each method. The SPL network is trained on a NVIDIA GeForce RTX 4060 GPU, and we run the BSF model in MATLAB R2023a on a 12th Gen Intel® Core™ i5-12450H processor at 2.00 GHz.

C. The effectiveness of SDR-BSF method

In this subsection, we aim to verify the effectiveness of the proposed SDR-BSF method. We initially verify the registration performance of the SDR method. Three well-known registration algorithms: the feature-based SIFT [15], the intensity-based NTG [16] and deep learning-based X-feat [17] are selected to perform band-wise registration for comparison. Table I records the evaluation metrics for the registered HSI obtained by compared methods on different datasets.

From the table, spatial domain registration approaches tend to exhibit a significant performance degradation with large scale factors. In contrast, the proposed SDR method remains

TABLE I
THE EVALUATION METRICS OF TEST IMAGE REGISTRATION METHODS.

Methods	SSIM	RMSE	SAM	TIME(s)
Faces (sf = 8, scaling)				
SIFT [15]	0.912	14.03	19.856	37
NTG [16]	0.924	12.55	17.056	152
X-feat [17]	0.907	14.18	20.615	23
SDR	0.963	3.52	11.140	8
Toys (sf = 32, pincushion)				
SIFT [15]	0.626	20.98	16.927	33
NTG [16]	0.759	15.35	23.323	147
X-feat [17]	0.699	18.36	20.156	22
SDR	0.965	3.88	11.695	6
Pavia U (sf = 4, rotation)				
SIFT [15]	0.737	16.84	6.544	25
NTG [16]	0.912	14.75	8.276	231
X-feat [17]	0.872	12.53	6.726	42
SDR	0.968	6.01	3.205	6
Pavia C (sf = 16, pincushion)				
SIFT [15]	0.616	18.69	16.776	23
NTG [16]	0.776	15.64	11.378	229
X-feat [17]	0.717	17.81	12.619	42
SDR	0.960	6.43	5.087	4

largely unaffected by significant scale factors (sf), which can be primarily attributed to the fact that the spectral information of HSIs is relatively insensitive to substantial sampling variations. Furthermore, the entire process of SDR only involves spectral super-resolution, without the need for feature point search and matching as required by SIFT and X-feat, or minimizing a loss function in an iterative algorithm form as with NTG. Therefore, the SDR method has a significantly lower computational time. Figure 6 shows the registration results of each method. As shown in the figure, the registered images produced by the compared methods exhibit more noticeable artifacts and distortions. In contrast, the image registered using the SDR method is highly consistent with the original image. The difference map of SDR is mainly concentrated along the edges, which is attributed to the smoothing effect of the convolutional neural network. However, since HSIs mainly provide spectral information, the lost texture details can be effectively compensated by the MSIs, and therefore do not compromise the subsequent fusion performance.

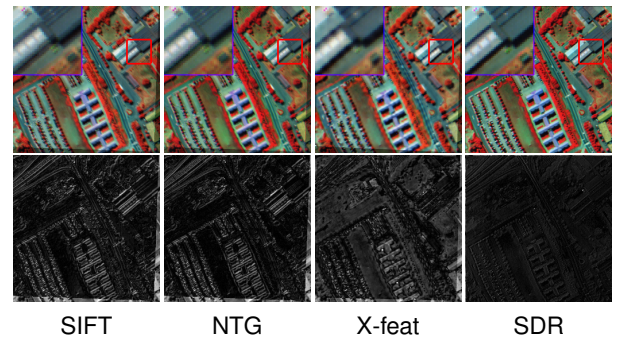


Fig. 6. The registration results for ‘Pavia University’ (bands 20, 40 and 60, sf = 4) dataset. The first row shows the blend image of the registered image and the original image, while the second row displays the difference image.

Next, we verify the overall registration and fusion performance of the SDR-BSF method. Specifically, we employ the blind fusion algorithm TriD [13] and ZSL [34] to fuse the pre-

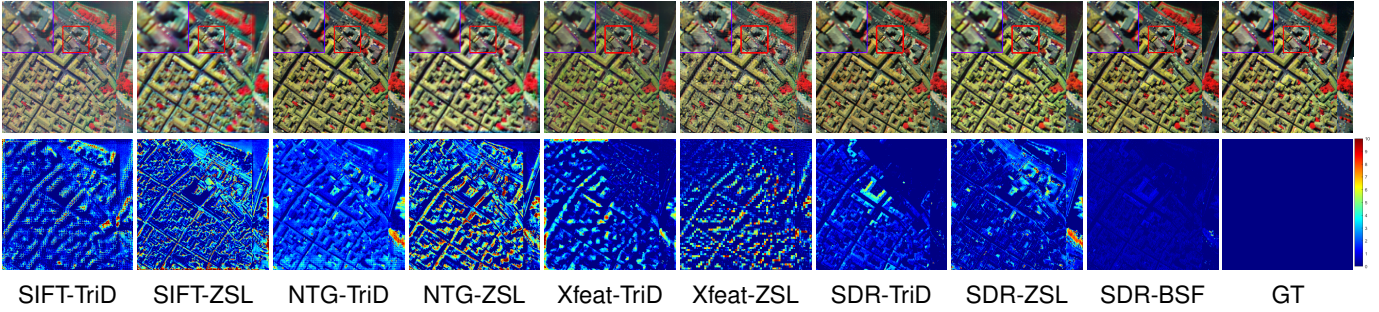


Fig. 7. The fused images and corresponding error images obtained by different methods for ‘Pavia Center’ (bands 20, 40 and 60, $\mathbf{sf} = 4$) dataset.

registered HSI-MSI pairs. As shown in Table II, the inadequate

TABLE II
THE EVALUATION METRICS FOR THE FUSED IMAGES.

Fusion		PSNR	SSIM	ERGAS	SAM
Pavia Center (sf = 4, scaling)					
SIFT	TriD [13]	31.96	0.927	5.364	7.70
	ZSL [34]	28.64	0.816	7.414	9.94
NTG	TriD [13]	31.47	0.933	5.984	7.82
	ZSL [34]	28.98	0.829	6.977	9.67
X-feat	TriD [13]	31.86	0.939	5.122	7.57
	ZSL [34]	29.63	0.843	6.737	8.91
SDR	TriD [13]	33.80	0.952	4.389	5.11
	ZSL [34]	32.26	0.935	5.146	7.24
	BSF	41.80	0.988	1.773	3.67
Superballs (sf = 16, pincushion)					
SIFT	TriD [13]	26.73	0.785	6.381	32.92
	ZSL [34]	26.35	0.776	6.773	33.26
NTG	TriD [13]	27.18	0.792	6.132	31.37
	ZSL [34]	26.46	0.779	7.196	33.85
X-feat	TriD [13]	28.40	0.806	6.151	28.35
	ZSL [34]	27.78	0.785	6.834	27.74
SDR	TriD [13]	33.96	0.925	4.238	22.74
	ZSL [34]	32.45	0.917	5.742	25.16
	BSF	39.78	0.960	1.565	10.09

registration accuracy of SIFT, NTG, and X-feat results in error accumulation during the subsequent estimation of the degradation operator and fusion stages, ultimately yielding suboptimal performance for these compared approaches. In contrast, the fusion methods achieve superior performance on the registered images obtained by SDR, which further validates the registration performance of our approach. Among the compared fusion techniques, TriD outperforms ZSL overall, which may due to TriD simultaneously conducts image registration and fusion, thereby minimizing error accumulation. Notably, the BSF model demonstrates significantly enhanced performance over both TriD and ZSL. This improvement can be attributed to the BSF model’s requirement to estimate only the spectral degradation operator \mathbf{R} , reducing the ill-posedness of the problem. Next, the fused images and corresponding error maps of the various methods are presented in Figure 7 for a visual comparison.

From the figure, the fusion images obtained using SIFT, NTG and X-feat registration exhibit errors primarily in the form of edge stripes and color discrepancies. These issues stem from accumulated errors during registration and degradation operator estimation. In contrast, the fusion images produced

with SDR registration show significantly fewer errors. However, the SDR-ZSL method still displays noticeable color differences because the degradation operator estimation in ZSL lacks prior regularization, making it less robust to misregistration. The reconstructed image generated by our SDR-BSF method demonstrates markedly fewer errors, thereby validating the effectiveness of our two-stage approach.

D. Comparison with other methods

1) *The experimental results on the simulated data:* We compare the performance of different methods under noisy conditions. The SNRh and SNRm are used to denote the signal-to-noise ratio of obtained HSI and MSI, respectively. We set SNRh = 35dB and SNRm = 40dB uniformly. Table III displays the experimental results of various methods on the ‘Pavia’ and the ‘CAVE’ datasets.

From the tables, ‘Hysure’ exhibits a certain level of robustness to misregistration despite not including a registration process. Its performance remains competitive when the scale factor is small. This suggests that Total Variation regularization can mitigate the impact of misalignment to some extent. The ‘Integrated’ method does not show ideal performance on all the datasets. A possible reason is that ‘Integrated’ relies entirely on optimization modeling. In scenarios where images are unregistered and degradation operators are unknown, there is insufficient known information and too many parameters to estimate. The vast solution space makes it challenging for the algorithm to find an optimal solution. The ‘NED’ adopts a method of registration followed by fusion, which may lead to accumulation of errors. Therefore, its reconstruction effect generally cannot achieve the optimal result. In summary, owing to insufficient information, model-driven methods tend to exhibit significant ill-posedness, leading to suboptimal performance. In contrast, deep learning-based methods generally achieve superior fusion performance, largely due to their powerful feature extraction capabilities and the ability to integrate registration and fusion modules synergistically. The ‘PMIRFCo’ method leverages multi-scale information within images, performing registration and fusion across multiple scales to achieve more precise alignment and enhanced fusion quality. The ‘NonregSR’ exhibits a slight performance advantage over the ‘Integrated’ approach. However, its effectiveness is unsatisfactory at higher scale factor, such as in the CAVE dataset. ‘DFMF’ relies on geolocation information for pre-registration, and for non-geographical HSIs, its fusion performance also demonstrates a competitive performance.

TABLE III
THE EXPERIMENTAL RESULTS OF COMPARED METHODS ON FIVE DATASETS UNDER DIFFERENT TRANSFORMATIONS.

Distortion		Scaling (1.1)				Rotation (2°)				Pincushion (1×10^{-2})			
Dataset	Method	PSNR	SSIM	ERGAS	SAM	PSNR	SSIM	ERGAS	SAM	PSNR	SSIM	ERGAS	SAM
Pavia C (sf = 4)	Hysure [12]	35.24	0.948	3.513	5.52	36.75	0.961	2.632	4.76	36.04	0.954	3.301	5.73
	Integrated [11]	31.85	0.904	5.558	6.36	32.40	0.916	5.104	6.19	31.68	0.897	5.359	6.82
	NED [39]	35.45	0.957	3.072	4.38	34.40	0.949	3.386	4.54	33.77	0.942	3.776	5.15
	NonregSR [9]	34.09	0.940	3.752	5.49	35.68	0.952	3.316	4.98	34.66	0.945	3.634	5.23
	PMIRFCo [49]	37.16	0.962	2.936	4.96	37.57	0.964	2.611	4.81	37.65	0.965	2.627	4.73
	DFMF [50]	38.56	0.974	2.234	4.14	38.11	0.972	2.274	4.26	38.48	0.974	2.226	4.21
	HPWRL [51]	37.62	0.963	2.551	4.63	37.80	0.963	2.578	4.59	37.44	0.961	2.775	4.68
	IR-ArF [52]	39.14	0.976	2.175	4.27	38.31	0.972	2.159	4.32	38.06	0.970	2.137	4.28
SDR-BSF	41.58	0.985	1.842	3.87	40.74	0.985	1.711	3.68	40.25	0.978	1.916	3.75	
Pavia U (sf = 8)	Hysure [12]	34.16	0.946	1.447	3.63	34.93	0.958	1.282	3.37	35.68	0.960	1.116	3.09
	Integrated [11]	30.24	0.868	3.382	5.35	31.33	0.879	3.159	5.16	31.76	0.875	3.574	4.84
	NED [39]	35.81	0.937	1.291	4.41	36.61	0.943	1.364	4.70	36.13	0.942	1.236	4.15
	NonregSR [9]	32.91	0.932	1.603	3.28	32.33	0.935	1.739	3.25	32.82	0.943	1.655	3.12
	PMIRFCo [49]	36.34	0.960	1.143	2.94	36.68	0.961	1.042	2.91	37.01	0.962	1.023	2.84
	DFMF [50]	36.92	0.965	1.072	3.55	37.21	0.969	0.973	3.46	36.40	0.959	1.150	3.73
	HPWRL [51]	35.47	0.962	1.470	3.71	35.16	0.966	1.322	3.72	35.99	0.968	1.310	3.64
	IR-ArF [52]	37.25	0.969	1.075	2.93	37.11	0.968	1.083	2.96	37.78	0.970	1.021	2.86
SDR-BSF	40.08	0.983	0.803	2.66	39.54	0.981	0.854	2.82	40.12	0.984	0.769	2.56	
Face (sf = 8)	Hysure [12]	34.65	0.893	2.957	17.36	35.01	0.906	2.826	16.90	34.88	0.901	2.916	16.79
	Integrated [11]	32.64	0.901	3.762	19.12	32.23	0.896	3.559	20.66	31.96	0.905	5.324	20.93
	NED [39]	36.78	0.959	2.032	16.85	36.97	0.960	1.983	16.59	36.39	0.956	2.557	15.41
	NonregSR [9]	34.61	0.948	3.352	16.52	35.25	0.884	2.471	15.76	34.47	0.944	3.490	17.14
	PMIRFCo [49]	37.47	0.960	2.436	13.84	37.96	0.961	2.267	13.86	36.82	0.961	2.786	14.32
	DFMF [50]	37.32	0.947	2.195	15.83	37.68	0.952	2.101	15.15	37.44	0.951	2.157	15.29
	HPWRL [51]	38.21	0.959	1.922	14.16	38.07	0.961	1.944	14.25	37.89	0.958	2.275	14.66
	IR-ArF [52]	39.43	0.971	1.879	13.75	39.36	0.971	1.884	13.94	38.77	0.968	2.063	14.15
SDR-BSF	41.28	0.975	1.625	12.51	41.56	0.976	1.610	11.86	40.82	0.969	1.818	12.44	
Superballs (sf = 16)	Hysure [12]	26.87	0.718	5.041	36.92	27.34	0.732	4.742	32.25	26.59	0.724	4.887	34.93
	Integrated [11]	28.17	0.743	4.739	34.98	28.35	0.752	4.652	31.92	27.78	0.748	4.663	32.29
	NED [39]	32.96	0.815	3.259	26.67	32.59	0.806	3.468	27.57	32.93	0.810	3.351	27.44
	NonregSR [9]	32.41	0.822	4.205	29.88	32.17	0.818	4.437	30.14	32.01	0.817	4.254	30.89
	PMIRFCo [49]	36.22	0.924	2.073	15.14	36.39	0.925	1.989	15.03	35.95	0.924	2.109	15.40
	DFMF [50]	35.64	0.912	2.415	16.85	36.47	0.923	2.389	15.60	36.15	0.920	2.426	16.28
	HPWRL [51]	35.21	0.918	2.689	15.58	36.14	0.935	2.301	14.89	35.73	0.927	2.570	15.32
	IR-ArF [52]	37.57	0.950	1.937	13.62	37.55	0.950	1.954	13.89	37.31	0.949	2.074	14.56
SDR-BSF	39.13	0.943	1.726	11.89	40.05	0.969	1.496	10.31	39.65	0.952	1.658	10.67	
Toys (sf = 32)	Hysure [12]	24.90	0.791	1.217	34.20	25.54	0.768	1.281	35.68	26.28	0.812	1.121	32.16
	Integrated [11]	27.72	0.906	1.169	22.14	28.91	0.909	1.086	22.07	29.23	0.905	1.067	22.40
	NED [39]	33.54	0.937	1.062	17.05	34.00	0.945	0.960	16.74	34.68	0.952	0.974	16.20
	NonregSR [9]	30.76	0.801	1.196	23.35	29.93	0.817	1.294	21.87	30.47	0.822	1.173	20.99
	PMIRFCo [49]	34.65	0.941	0.897	16.43	35.42	0.946	0.972	21.71	34.27	0.911	3.471	15.74
	DFMF [50]	35.67	0.947	0.934	14.74	35.83	0.947	0.879	15.27	36.08	0.948	0.933	15.49
	HPWRL [51]	33.68	0.943	1.068	16.96	34.16	0.945	1.045	16.59	33.35	0.942	1.027	17.11
	IR-ArF [52]	35.02	0.945	0.916	15.37	34.95	0.944	0.923	15.54	35.27	0.947	0.881	15.07
SDR-BSF	37.85	0.954	0.699	13.05	38.03	0.954	0.733	13.21	38.19	0.954	0.658	12.96	

‘HPWRL’ achieved better reconstruction performance when the scale factor is small. ‘IR-ArF’ overall demonstrates strong competitiveness. It translates each step of the optimization algorithm into deep network modules and jointly incorporates implicit neural networks to flexibly adjust the image resolution. However, it still lacks robustness in the case of large scale factors. In comparison, our method consistently achieves optimal restoration performance, which is mainly owing to the innovative strategy of using spectral super-resolution on the MSI to obtain registered images. Local misregistration and significant downsampling primarily degrade the spatial information of HSIs, with considerably less impact on spectral information. Consequently, our spectral reconstruction-based approach demonstrates exceptional robustness. Additionally, the BSF method effectively leverages prior information from

the images, delivering excellent semi-blind fusion performance while reducing computational costs. Next, we display the reconstructed images and corresponding error maps for each method in Figure 8.

As shown in the figures, ‘Hysure’ exhibits noticeable color differences and stripes on the ‘CAVE’ dataset, although its performance on the ‘Pavia’ dataset is relatively superior. The reconstructed images from ‘Integrated’ and ‘NED’ also show significant distortions and color discrepancies in the ‘CAVE’ dataset. These issues primarily stem from inaccuracies in the estimation of the degradation operators \mathbf{B} and \mathbf{R} . In summary, model-driven methods tend to perform less effectively at larger scale factors. ‘NonregSR’ performs well on the ‘Pavia’ dataset but exhibits noticeable flaws on the ‘CAVE’. This may be due to a significant decrease in registration performance when the

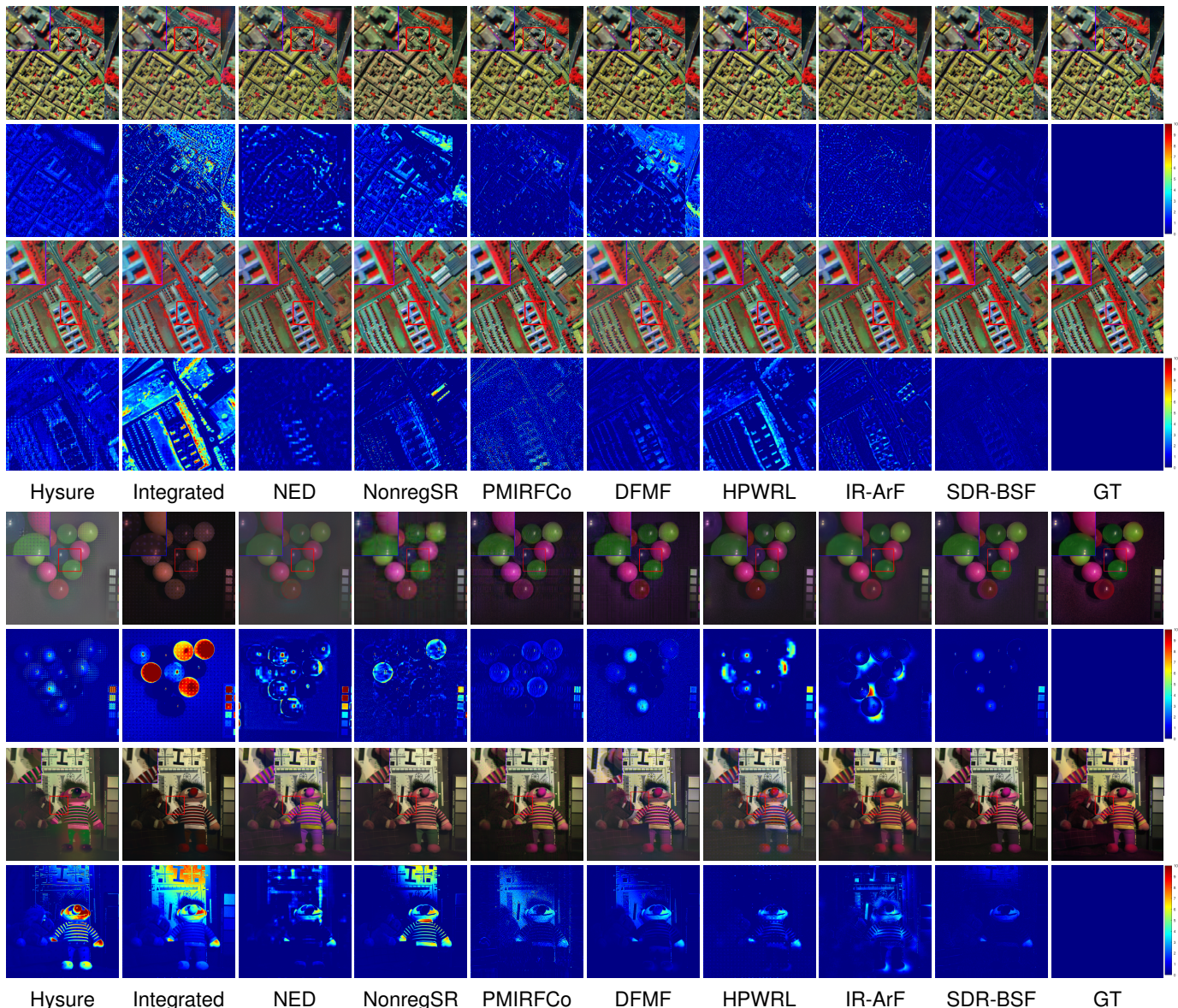


Fig. 8. Visualization of the fused images and error maps for the ‘Pavia’ (bands 20, 40 and 60) and ‘CAVE’ (bands 10, 20, and 30) datasets. The ‘Pavia Center’ and ‘Superballs’ images undergo scaling distortion, whereas the ‘Pavia University’ and ‘Toys’ dataset undergo pincushion transformation.

scale factor is large, which subsequently leads to suboptimal fusion performance. In comparison, ‘PMIRFCo’ exhibits significantly fewer flaws, which can be attributed to its multi-scale learning approach. This method fully exploits image details and enhances the network’s learning accuracy, resulting in superior performance. The reconstruction images from ‘DFMF’ also show slight distortions, likely due to less precise estimation of degradation operators when registration and degradation are estimated simultaneously. The fused images of the ‘Superballs’ using the ‘HPWRL’ method display localized distortions. From the error map, it can be seen that the defects of ‘IR-ArF’ are mainly concentrated in the edge regions of the image. This also indicates that the registration performance of ‘IR-ArF’ is not robust enough under large spatial scale factors. In contrast, the SDR-BSF method leverages spectral super-resolution, ensuring high-quality fusion as long as the spectral information is complete, which allows to maintain robust performance even at larger scale factors. Consequently,

our method produces fused images with higher quality and notably fewer artifacts in the error maps compared to other methods, which verifies the effectiveness of our approach.

2) *The experimental results on real-world data:* Next, we validate the effectiveness of the proposed SDR-BSF method on real-world datasets: GF1-GF5 and FR2. The image pairs are not pre-registered, and the degradation operators remain unidentified. Due to the absence of a ground truth image, we assess the effectiveness of different methods by examining image details. We display the recovery performance of each compared method on the GF1-GF5 dataset in Figure 9.

In the input MSI and the fused images, a ‘vortex’ feature is highlighted with a red square, while a specific pattern detail is indicated by a blue border and magnified in the top-left corner of the image. Meanwhile, yellow squares are used to mark areas for the comparison of spectral differences. The ‘Integrated’ method also shows significant color discrepancies, indicating potential biases in the spectral information.

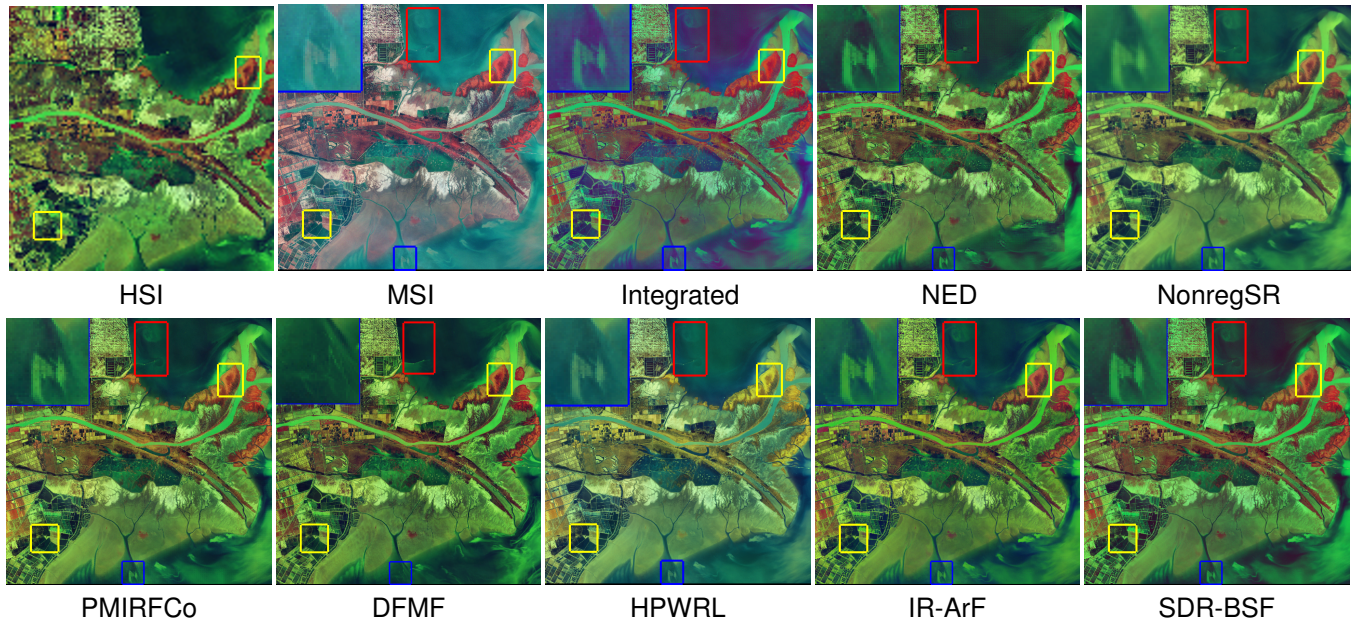


Fig. 9. Visualization of the fused images for the GF1-GF5 datasets (bands 30, 60 and 90) using various compared methods.

Additionally, the fused image obtained from ‘NED’ displays a noticeable sense of discontinuity at the common scene boundaries. In comparison, the reconstruction image obtained by ‘NonregSR’ shows some blurriness and is accompanied by slight color differences. Intuitively, ‘PMIRFCo’ achieves superior restoration performance while retaining important image details. However, the enlarged view reveals that the fused image suffers from slight distortion. ‘HPWRL’ performs well in the spatial dimension. However, there are obvious color differences compared to the original HSI. The reconstruction images from ‘DFMF’ are obtained by first performing pre-registration of the HSI and MSI using geolocation coordinates, followed by the ‘DFMF’ method. As can be seen, ‘DFMF’ achieves high-quality reconstruction overall. Nevertheless, some textural details in the reconstruction images are smoothed out at the locations marked in red and blue. Visually, ‘IR-ArF’ produces a higher-quality fused image. In contrast, the proposed SDR-BSF method retains important image details while exhibiting less color differences, which validates the effectiveness of our approach on real dataset.

Figure 10 displays the restored images from each method on the FR2 dataset, with the blue and yellow regions magnified for closer inspection. This dataset contains highly complex scenes, which result in relatively noticeable distortions in the fused images across various methods. The methods ‘NED’, ‘PMIRFCo’, and ‘DFMF’ do not exhibit noticeable color differences in their fused images. However, upon closer inspection of the magnified regions, it is evident that these images suffer from varying degrees of spatial distortion. One possible reason for this is the complexity of the scenes in the FR2 dataset, which makes it challenging to achieve high-quality recovery of spatial information. The fused image from ‘Integrated’, ‘NonregSR’ and ‘HPWRL’ exhibit color differences, and some important details in the red region have been smoothed out. The fused image of ‘IR-ArF’ exhibits stripe distortions. In contrast, the fused image obtained from our method, while exhibiting slight color differences, retains

important details and displays clearer spatial textures. This further validates the effectiveness of our approach.

E. Running time

Next, we compare the runtime of each algorithm in Table IV. From the table, ‘Hysure’ and ‘NED’ are competitive in

TABLE IV
THE TIME CONSUMPTION OF THE COMPARED METHODS (UNIT: SECONDS).

dataset	Pavia C	Superballs	GF1-GF5	FR2
Hysure [12]	47	69	124	84
Integrated [11]	260	373	757	526
NED [39]	24	33	51	44
NonregSR [9]	931	1225	3560	3030
PMIRFCo [49]	438	562	1275	913
DFMF [50]	259	501	1065	845
HPWRL [51]	254	341	863	684
IR-ArF [52]	669	854	2630	2460
SDR-BSF	10	13	17	14

terms of computational efficiency since they do not require a training phase. Instead, the majority of their computational time is dedicated to iterative solving processes. The compared deep learning-based methods tend to take longer processing time. This is mainly due to the fact that these methods tackle the problem from the spatial dimension, which necessitates the inclusion of complex registration and fusion modules, as well as degradation operator estimation modules. This makes the training process intricate and time-consuming. In contrast, our method obtains registered images from the perspective of spectral super-resolution, and the designed network is very concise. Moreover, the BSF model does not involve computationally intensive steps. Consequently, the time consumption is significantly lower than that of other comparative methods.

F. Ablation study

Next, we conduct ablation studies to evaluate the effectiveness of our innovations. For the SPL network, we validate the

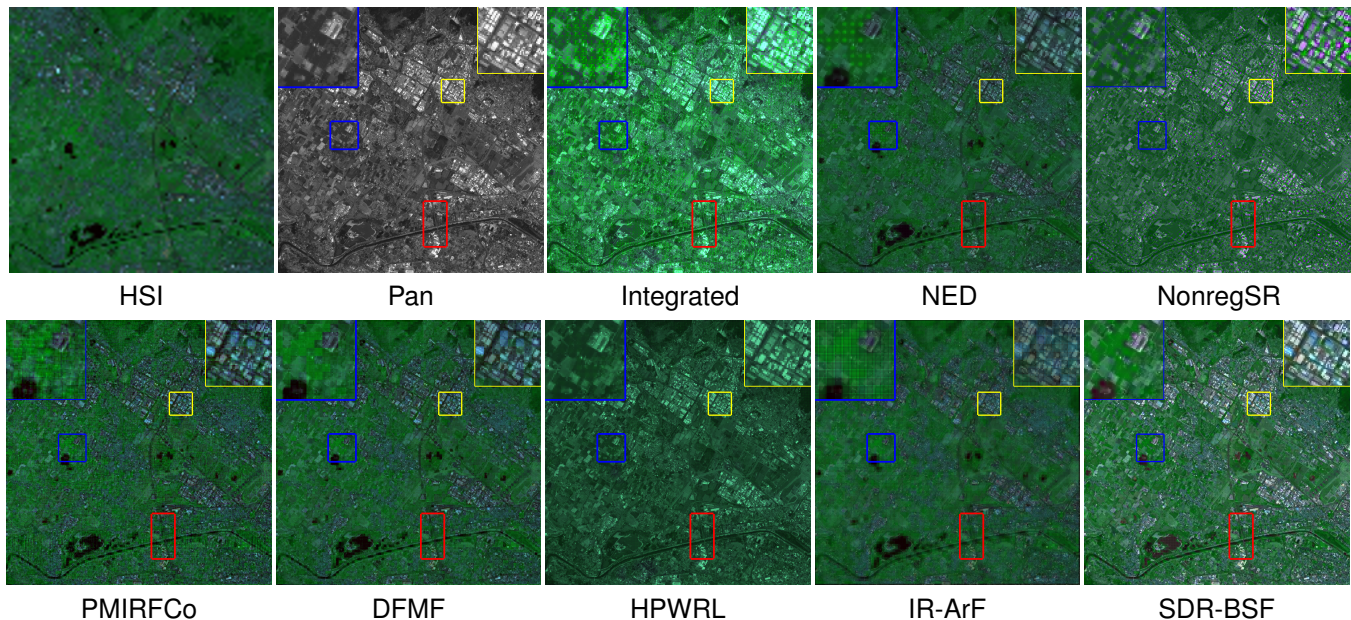


Fig. 10. Visualization of the fused images for the FR2 datasets (bands 15, 30 and 45) using various compared methods.

efficacy of the subspace representation (SR) method and the cyclic training strategy (CTS) in Figure 11 and 12.

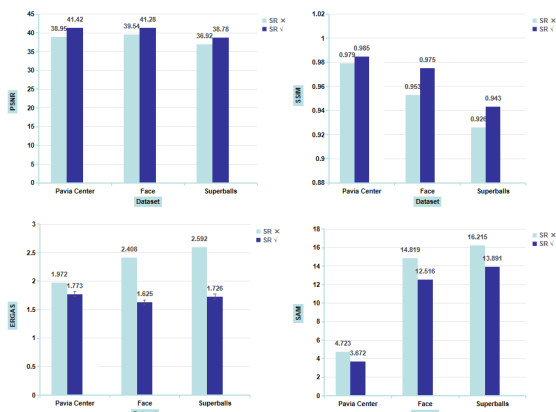


Fig. 11. Ablation experiment for the subspace representation (SR) under scaling transformation for different HSI datasets.

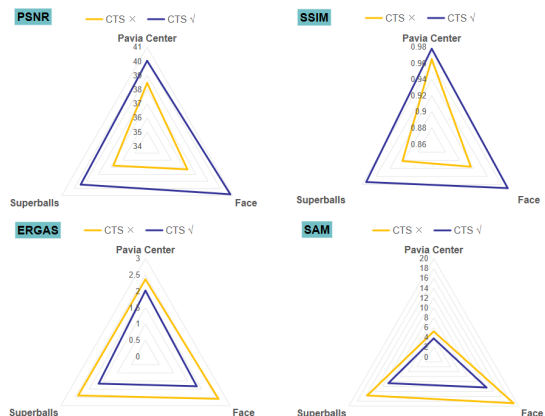


Fig. 12. Ablation experiment for the cyclic training strategy (CTS) under pincushion transformation for different HSI datasets.

Figure 11 demonstrates that the SR approach has a positive impact on the registration and fusion process for all

the three datasets. For example, it improved the PSNR of the fused image by nearly 2.5 dB for ‘Pavia Center’ dataset. Other evaluation metrics also showed significant improvements across different datasets, which verifies the effectiveness of the SR method. Figure 12 shows that cyclic training strategy can decrease the spectral deviation caused by unregistered original image pairs. We focused on the SAM metric and found that CTS showed a significant improvement for all the three datasets. This indicates that CTS can effectively enhance the spectral reconstruction accuracy of fused images.

G. The influence of fusion on classification accuracy

To demonstrate the effectiveness of the SDR-BSF approach in subsequent downstream tasks, we evaluate its impact on classification accuracy using the Houston dataset [58]. This dataset comprises a spatial resolution of 349×1905 pixels and 144 spectral bands. We chose spectral bands 11 through 110 and average every 25 bands to obtain the MSI. The HSI is generated by applying an 7×7 Gaussian kernel with a standard deviation of 2 and a downsampling ratio of 8. Furthermore, we applied a 2° rotation to the HSI and performed a barrel transformation to misalign it with the MSI. Subsequently, the fused image was obtained using the SDR-BSF model. Then, we classified the HSI, MSI and the fused image using the SVM-KC algorithm [59]. Table V presents the classification outcomes, highlighting both the accuracy for each category and the overall average accuracy. The classification performance for most categories on the fused HSI surpasses that of the HSI and MSI. Notably, the average accuracy for the predicted HR-HSI is 12.1% higher than the HSI and 3.8% higher than MSI. This validates the effectiveness of our method in enhancing HSI classification performance.

V. CONCLUSION

In this paper, we proposed the SDR-BSF method to address the blind fusion challenge of unregistered HSI-MSI pairs. We

TABLE V
CLASSIFICATION RESULTS OF LR-HSI AND FUSED HSI (ACCURACY(%)).

Category	HSI	MSI	Fused HSI
Healthy grass	70	92	92
Stressed grass	67	95	94
Synthetic grass	71	99	99
Trees	60	96	97
Soil	76	86	88
Water	72	95	95
Residential	54	68	72
Commercial	72	49	74
Road	66	72	72
Highway	84	69	86
Railway	84	76	82
Parking lot 1	71	67	70
Parking lot 2	62	63	63
Tennis court	96	93	97
Running track	87	96	97
Average	72.8	81.1	84.9

innovatively propose to perform registration in the spectral domain, achieving HSI registration by applying spectral super-resolution to the MSI. Through cyclic training and subspace representation methods, we acquire higher quality and more robust registration performance. Next, the semi-blind BSF model is developed to fuse the registered images, which leverages group sparsity to characterize the low-rank property of the image. This approach eliminates the need for computationally expensive SVD. We solve the BSF model using PAO algorithm and provide its detailed convergence analysis. Finally, extensive numerical experiments are conducted to verify the effectiveness of our approach.

REFERENCES

- [1] D. Landgrebe, "Hyperspectral image data analysis," *IEEE Signal Proc. Mag.*, vol. 19, no. 1, pp. 17–28, Aug. 2002.
- [2] M. Lv, W. Li, T. Chen, J. Zhou, and R. Tao, "Discriminant tensor-based manifold embedding for medical hyperspectral imagery," *IEEE J. Biomed. Health Informat.*, vol. 25, no. 9, pp. 3517–3528, Sep. 2021.
- [3] X. He, J. Wu, Q. Ling, Z. Li, Z. Lin, and S. Zhou, "Anomaly detection for hyperspectral imagery via tensor low-rank approximation with multiple subspace learning," *IEEE Trans. Geosci. Remote Sens.*, vol. 61, pp. 1–17, Apr. 2023.
- [4] Z. Xie, J. Hu, X. Kang, and P. Duan, "Multilayer global spectral-spatial attention network for wetland hyperspectral image classification," *IEEE Trans. Geosci. Remote Sens.*, vol. 60, pp. 1–13, Feb. 2022.
- [5] F. A. Mianji, Y. Zhang, H. K. Sulehria, A. Babakhani, and M. R. Kardan, "Super-resolution challenges in hyperspectral imagery," *Inf. Technol. J.*, vol. 7, no. 7, pp. 1030–1036, Jul. 2008.
- [6] M. Rostami and A. A. Beheshti Shirazi, "Hyperspectral image super-resolution via learning an undercomplete dictionary and intra-algorithmic postprocessing," *IEEE Trans. Geosci. Remote Sens.*, vol. 61, pp. 1–15, 2023.
- [7] L. Loncan, L. B. de Almeida, J. M. Bioucas-Dias, X. Briottet, J. Chanussot, N. Dobigeon, S. Fabre, W. Liao, G. A. Licciardi, M. Simoes, J.-Y. Tourneret, M. A. Veganzones, G. Vivone, Q. Wei, and N. Yokoya, "Hyperspectral pansharpening: A review," *IEEE Geosci. Remote Sens. Mag.*, vol. 3, no. 3, pp. 27–46, Sep. 2015.
- [8] K. Ren, W. Sun, X. Meng, G. Yang, J. Peng, J. Huang, and J. Li, "Cdfls: Image registration for spaceborne hyperspectral and multispectral data having large spatial-resolution difference," *IEEE Trans. Geosci. Remote Sens.*, vol. 61, pp. 1–15, 2023.
- [9] K. Zheng, L. Gao, D. Hong, B. Zhang, and J. Chanussot, "Nonregsmet: A nonrigid registration hyperspectral super-resolution network," *IEEE Trans. Geosci. Remote Sens.*, vol. 60, pp. 1–16, 2022.
- [10] Y. Qu, H. Qi, C. Kwan, N. Yokoya, and J. Chanussot, "Unsupervised and unregistered hyperspectral image super-resolution with mutual dirichlet-net," *IEEE Trans. Geosci. Remote Sens.*, vol. 60, pp. 1–18, 2022.
- [11] Y. Zhou, A. Rangarajan, and P. D. Gader, "An integrated approach to registration and fusion of hyperspectral and multispectral images," *IEEE Trans. Geosci. Remote Sens.*, vol. 58, no. 5, pp. 3020–3033, May 2020.
- [12] M. Simões, J. Bioucas-Dias, L. B. Almeida, and J. Chanussot, "A convex formulation for hyperspectral image superresolution via subspace-based regularization," *IEEE Trans. Geosci. Remote Sens.*, vol. 53, no. 6, pp. 3373–3388, Jun. 2015.
- [13] K. Yang, M. Bai, R. Dian, and T. Lu, "Subspace-based coupled tensor decomposition for hyperspectral blind fusion," *Inverse Probl. Imaging*, vol. 19, no. 3, pp. 560–591, 2025.
- [14] R. Dian and S. Li, "Hyperspectral image super-resolution via subspace-based low tensor multi-rank regularization," *IEEE Trans. Image Process.*, vol. 28, no. 10, pp. 5135–5146, Aug. 2019.
- [15] D. G. Lowe, "Distinctive image features from scale-invariant keypoints," *Int. J. Comput. Vis.*, vol. 60, no. 2, pp. 91–110, Nov. 2004.
- [16] S.-J. Chen, H.-L. Shen, C. Li, and J. H. Xin, "Normalized total gradient: A new measure for multispectral image registration," *IEEE Trans. Image Process.*, vol. 27, no. 3, pp. 1297–1310, Mar. 2018.
- [17] G. Potje, F. Cadar, A. Araujo, R. Martins, and E. R. Nascimento, "Xfeat: Accelerated features for lightweight image matching," in *IEEE Conf. Comput. Vis. Pattern Recog. (CVPR)*. IEEE, Jun. 2024, pp. 2682–2691.
- [18] T. Xu, T.-Z. Huang, L.-J. Deng, and N. Yokoya, "An iterative regularization method based on tensor subspace representation for hyperspectral image super-resolution," *IEEE Trans. Geosci. Remote Sens.*, vol. 60, pp. 1–16, May 2022.
- [19] N. Yokoya, T. Yairi, and A. Iwasaki, "Coupled nonnegative matrix factorization unmixing for hyperspectral and multispectral data fusion," *IEEE Trans. Geosci. Remote Sens.*, vol. 50, no. 2, pp. 528–537, Feb. 2012.
- [20] W. Dong, F. Fu, G. Shi, X. Cao, and J. Wu, "Hyperspectral image super-resolution via non-negative structured sparse representation," *IEEE Trans. Image Process.*, vol. 25, no. 5, pp. 2337–2352, May 2016.
- [21] X. Zhao, M. Bai, D. Sun, and L. Zheng, "Robust tensor completion: Equivalent surrogates, error bounds, and algorithms," *SIAM J. Imaging Sci.*, vol. 15, no. 2, pp. 625–669, May 2022.
- [22] C. I. Kanatsoulis, X. Fu, N. D. Sidiropoulos, and W.-K. Ma, "Hyperspectral super-resolution: A coupled tensor factorization approach," *IEEE Trans. Signal Process.*, vol. 66, no. 24, pp. 6503–6517, Dec. 2018.
- [23] J. Zeng, G. Zhou, Y. Qiu, Y. Ma, and Q. Zhao, "Hyperspectral and multispectral image fusion via bayesian nonlocal cp factorization," *IEEE Geosci. Remote Sens. Letters*, vol. 21, pp. 1–5, Dec. 2023.
- [24] S. Li, R. Dian, L. Fang, and J. M. Bioucas-Dias, "Fusing hyperspectral and multispectral images via coupled sparse tensor factorization," *IEEE Trans. Image Process.*, vol. 27, no. 8, pp. 4118–4130, Aug. 2018.
- [25] X. Li, Y. Yuan, and Q. Wang, "Hyperspectral and multispectral image fusion via nonlocal low-rank tensor approximation and sparse representation," *IEEE Trans. Geosci. Remote Sens.*, vol. 59, no. 1, pp. 550–562, Jan. 2021.
- [26] Y. Xu, Z. Wu, J. Chanussot, and Z. Wei, "Nonlocal patch tensor sparse representation for hyperspectral image super-resolution," *IEEE Trans. Image Process.*, vol. 28, no. 6, pp. 3034–3047, Jun. 2019.
- [27] L. Gao, J. Li, K. Zheng, and X. Jia, "Enhanced autoencoders with attention-embedded degradation learning for unsupervised hyperspectral image super-resolution," *IEEE Trans. Geosci. Remote Sens.*, vol. 61, pp. 1–17, 2023.
- [28] S. Liu, T. Shao, S. Liu, B. Li, and Y.-D. Zhang, "An asymptotic multiscale symmetric fusion network for hyperspectral and multispectral image fusion," *IEEE Trans. Geosci. Remote Sens.*, vol. 63, pp. 1–16, 2025.
- [29] F. Palsson, J. R. Sveinsson, and M. O. Ulfarsson, "Multispectral and hyperspectral image fusion using a 3-d-convolutional neural network," *IEEE Geosci. Remote Sens. Lett.*, vol. 14, no. 5, pp. 639–643, May 2017.
- [30] R. Dian, S. Li, and X. Kang, "Regularizing hyperspectral and multispectral image fusion by cnn denoiser," *IEEE Trans. Neural Netw. Learn. Syst.*, vol. 32, no. 3, pp. 1124–1135, Mar. 2021.
- [31] Q. Xie, M. Zhou, Q. Zhao, Z. Xu, and D. Meng, "MHF-net: An interpretable deep network for multispectral and hyperspectral image fusion," *IEEE Trans. Pattern Anal. Mach. Intell.*, vol. 44, no. 3, pp. 1457–1473, Mar. 2022.

- [32] X. Wang, C. Cheng, S. Liu, R. Song, X. Wang, and L. Feng, "Ss-inr: Spatial-spectral implicit neural representation network for hyperspectral and multispectral image fusion," *IEEE Trans. Geosci. Remote Sens.*, vol. 61, pp. 1–14, 2023.
- [33] Y. Liu, R. Dian, and S. Li, "Low-rank transformer for high-resolution hyperspectral computational imaging," *Int. J. Comput. Vis.*, Aug. 2024.
- [34] R. Dian, A. Guo, and S. Li, "Zero-shot hyperspectral sharpening," *IEEE Trans. Pattern Anal. Mach. Intell.*, pp. 1–17, May 2023.
- [35] J. Li, K. Zheng, J. Yao, L. Gao, and D. Hong, "Deep unsupervised blind hyperspectral and multispectral data fusion," *IEEE Geosci. Remote Sens. Letters*, vol. 19, pp. 1–5, 2022.
- [36] L. Zhang, J. Nie, W. Wei, and Y. Zhang, "Unsupervised test-time adaptation learning for effective hyperspectral image super-resolution with unknown degeneration," *IEEE Trans. Pattern Anal. Mach. Intell.*, vol. 46, no. 7, pp. 5008–5025, Jul. 2024.
- [37] H. Wang, Y. Xu, Z. Wu, and Z. Wei, "Unsupervised hyperspectral and multispectral image blind fusion based on deep tucker decomposition network with spatial-spectral manifold learning," *IEEE Trans. Neural Netw. Learn. Syst.*, pp. 1–15, 2024.
- [38] Y. Fu, Y. Zheng, L. Zhang, and Y. Zheng, "Simultaneous hyperspectral image super-resolution and geometric alignment with a hybrid camera system," *Neurocomputing*, vol. 384, pp. 282–294, Apr. 2020.
- [39] J. Ying, H.-L. Shen, and S.-Y. Cao, "Unaligned hyperspectral image fusion via registration and interpolation modeling," *IEEE Trans. Geosci. Remote Sens.*, vol. 60, pp. 1–14, 2022.
- [40] G. Balakrishnan, A. Zhao, M. R. Sabuncu, J. Guttag, and A. V. Dalca, "Voxelmorph: A learning framework for deformable medical image registration," *IEEE Trans. Med. Imag.*, vol. 38, no. 8, pp. 1788–1800, Aug. 2019.
- [41] Y. Guo, X. Fu, M. Xu, and S. Jia, "Stereo cross-attention network for unregistered hyperspectral and multispectral image fusion," *IEEE Trans. Geosci. Remote Sens.*, vol. 61, pp. 1–15, 2023.
- [42] J. Qu, J. Cui, W. Dong, Q. Du, X. Wu, S. Xiao, and Y. Li, "A principle design of registration-fusion consistency: Toward interpretable deep unregistered hyperspectral image fusion," *IEEE Trans. Neural Netw. Learn. Syst.*, pp. 1–15, 2024.
- [43] T. G. Kolda and B. W. Bader, "Tensor decompositions and applications," *SIAM Review*, vol. 51, no. 3, pp. 455–500, Aug. 2009.
- [44] D. P. Kingma and J. Ba, "Adam: A method for stochastic optimization," *arXiv:1412.6980*, Dec. 2014.
- [45] V. Sitzmann, J. N. P. Martel, A. W. Bergman, D. B. Lindell, and G. Wetzstein, "Implicit neural representations with periodic activation functions," Jun. 2020.
- [46] W. Li, W. Bian, and K.-C. Toh, "On solving a rank regularized minimization problem via equivalent factorized column-sparse regularized models," *Math. Program.*, Jul. 2024.
- [47] L. Pan and X. Chen, "Group sparse optimization for images recovery using capped folded concave functions," *SIAM J. Imaging Sci.*, vol. 14, no. 1, pp. 1–25, Jan. 2021.
- [48] E. J. Candès, X. Li, Y. Ma, and J. Wright, "Robust principal component analysis?" *J. ACM*, vol. 58, no. 3, pp. 1–37, May 2011.
- [49] J. Qu, X. Liu, W. Dong, Y. Liu, T. Zhang, Y. Xu, and Y. Li, "Progressive multi-iteration registration-fusion co-optimization network for unregistered hyperspectral image super-resolution," *IEEE Trans. Geosci. Remote Sens.*, vol. 62, pp. 1–14, 2024.
- [50] A. Guo, R. Dian, and S. Li, "A deep framework for hyperspectral image fusion between different satellites," *IEEE Trans. Pattern Anal. Mach. Intell.*, pp. 1–16, 2022.
- [51] J. Nie, W. Wei, L. Zhang, C. Ding, and Y. Zhang, "Hybrid pixel-wise registration learning for robust fusion-based hyperspectral image super-resolution," *IEEE Trans. Comput. Imaging*, vol. 10, pp. 915–927, 2024.
- [52] J. Qu, X. Wu, W. Dong, J. Cui, and Y. Li, "Ir&arf: Toward deep interpretable arbitrary resolution fusion of unregistered hyperspectral and multispectral images," *IEEE Trans. Image Process.*, vol. 34, pp. 1934–1949, 2025.
- [53] F. Dell'Acqua, P. Gamba, A. Ferrari, J. Palmason, J. Benediktsson, and K. Arnason, "Exploiting spectral and spatial information in hyperspectral urban data with high resolution," *IEEE Geosci. Remote Sens. Lett.*, vol. 1, no. 4, pp. 322–326, Oct. 2004.
- [54] Q. Wei, N. Dobigeon, and J.-Y. Tourneret, "Fast fusion of multi-band images based on solving a sylvester equation," *IEEE Trans. Image Process.*, vol. 24, no. 11, pp. 4109–4121, Jul. 2015.
- [55] G. Vivone, A. Garzelli, Y. Xu, W. Liao, and J. Chanussot, "Panchromatic and hyperspectral image fusion: Outcome of the 2022 whispers hyperspectral pansharpening challenge," *IEEE J. Sel. Top. Appl. Earth Observ. Remote Sens.*, vol. 16, pp. 166–179, 2023.
- [56] Z. Wang, A. Bovik, H. Sheikh, and E. Simoncelli, "Image quality assessment: from error visibility to structural similarity," *IEEE Trans. Image Process.*, vol. 13, no. 4, pp. 600–612, Apr. 2004.
- [57] Q. Wei, J. Bioucas-Dias, and N. Dobigeon, "Hyperspectral and multispectral image fusion based on a sparse representation," *IEEE Trans. Geosci. Remote Sens.*, vol. 53, no. 7, pp. 3658–3668, Jul. 2015.
- [58] C. Debes and A. Merentitis, "Hyperspectral and lidar data fusion: Outcome of the 2013 grss data fusion contest," *IEEE J. Sel. Top. Appl. Earth Observ. Remote Sens.*, vol. 7, no. 6, pp. 2405–2418, Jun. 2014.
- [59] G. Camps-Valls, L. Gomez-Chova, J. Munoz-Mari, J. Vila-Frances, and J. Calpe-Maravilla, "Composite kernels for hyperspectral image classification," *IEEE Geos. Remote Sens. Lett.*, vol. 3, no. 1, pp. 93–97, Jan. 2006.